

Electronic State Unfolding for Plane Waves: Energy Bands, Fermi Surfaces, and Spectral Functions

Published as part of The Journal of Physical Chemistry virtual special issue "D. D. Sarma Festschrift".

David Dirnberger, Georg Kresse, Cesare Franchini, and Michele Reticcioli*

Cite This: *J. Phys. Chem. C* 2021, 125, 12921–12928

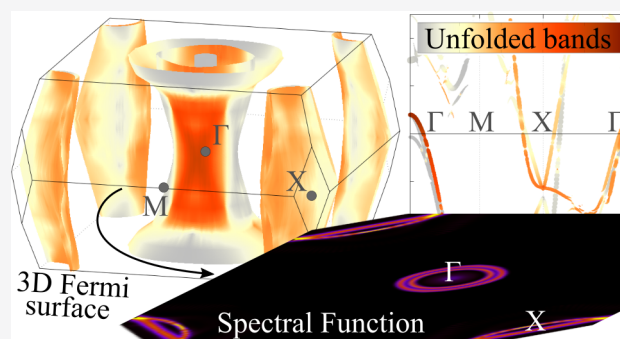
Read Online

ACCESS |

Metrics & More

Article Recommendations

ABSTRACT: Present day computing facilities allow for first-principles density functional theory studies of complex physical and chemical phenomena. Often such calculations are linked to large supercells to adequately model the desired property. However, supercells are associated with small Brillouin zones in the reciprocal space, leading to folded electronic eigenstates that make the analysis and interpretation extremely challenging. Various techniques have been proposed and developed to reconstruct the electronic band structures of super cells unfolded into the reciprocal space of an ideal primitive cell. Here we propose an unfolding scheme embedded directly in the Vienna *Ab initio* Simulation Package (VASP) that requires modest computational resources and allows for an automatized mapping from the reciprocal space of the supercell to the primitive cell Brillouin zone. This algorithm can compute band structures, Fermi surfaces, and spectral functions by using an integrated postprocessing tool (bands4vasp). Here the method is applied to a selected variety of complex physical situations: the effect of doping on the band dispersion in the $\text{BaFe}_{2(1-x)}\text{Ru}_{2x}\text{As}_2$ superconductor, the interaction between adsorbates and polaronic states on the $\text{TiO}_2(110)$ surface, and the band splitting induced by noncollinear spin fluctuations in EuCd_2As_2 .



1. INTRODUCTION

Material science simulations adopting periodic boundary conditions in the framework of the density functional theory (DFT) may require large unit cells to model long or broken periodicity in crystals. Supercells (i.e., large unit cells built by the stacking of smaller primitive cells forming an ideal Bravais lattice) are used to study the effects of lattice impurities (e.g., local dislocations, defects, doping) and also to investigate domain boundaries, magnetic orders, surface reactivity, and structural reconstructions, just to name a few common applications.^{1,2} Whereas well-developed facilities and efficient DFT packages are capable of dealing with hundreds and even thousands of atoms in large cells, the analysis of the electronic properties (such as the energy band structure or the Fermi surface) gets complicated by the shrinking of the Brillouin zone (BZ) and the consequent folding of the eigenstates in the reciprocal space.³ This also prevents a genuine comparison with photoemission spectroscopy experiments.^{4,5}

Figure 1 shows an example of the intricate band structure typically obtained by using a supercell. Clearly, the bands calculated by using the primitive cell instead allow for a more straightforward analysis. The intricate supercell states can be unfolded back into the larger BZ of the primitive cell by applying the unfolding technique.^{3,6–10} This technique is based

on the projection P_{K_m} of the supercell eigenstates $|K_m\rangle$ on the primitive cell eigenstates $|k_n\rangle$

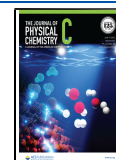
$$P_{K_m}(\mathbf{k}_i) = \sum_n |\langle K_m | \mathbf{k}_i \rangle|^2 \quad (1)$$

where m and n denote energy band indices at vectors \mathbf{K} and \mathbf{k} , in the reciprocal space of the supercell and the primitive cell, respectively. This projection represents the amount of Bloch character of the states $|k_n\rangle$ contributing to $|K_m\rangle$, which allows for a direct connection between the reciprocal space of the supercell and the primitive cell: This assignment is straightforward for supercells built as a perfect stacking of the primitive cell because the Bloch character is zero for all but one $|k_n\rangle$ state; conversely, nontrivial supercells modeling deviations from the primitive cell symmetry (induced by, for example, impurities and disorder) show faded Bloch

Received: March 15, 2021

Revised: May 26, 2021

Published: June 9, 2021



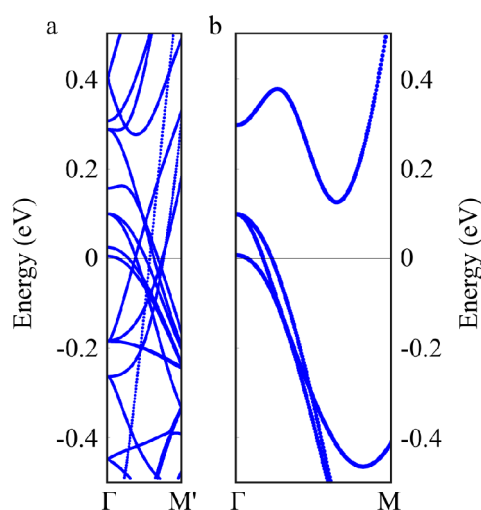


Figure 1. Example of eigenstate folding for the pristine BaFe₂As₂ compound. Band structures obtained by using (a) a supercell and (b) a primitive cell.

characters, with multiple contributions from the primitive cell states to the $|K_m\rangle$ state. By weighting the contributions of all single states with P_{K_m} , it is indeed possible to obtain an effective band structure (EBS) of the supercell unfolded in the larger BZ of the primitive cell.

If the eigenstates $|K_m\rangle$ are expanded in terms of a plane-wave basis set with coefficients $C_{m,K}$, then eq 1 can be rewritten in terms of states of the supercell only¹¹

$$P_{K_m}(k_i) = \sum_{\{g\}} |C_{m,g+k_i}|^2 \quad (2)$$

By expressing P_{K_m} in this form, all information required from the primitive cell is purely geometric and collected by the reciprocal lattice vector g applied to the k_i vectors in the reciprocal space. This alternative formulation has the advantage of avoiding any calculation on the primitive cell as well as any direct comparison between the two spaces, which could turn out to be technically challenging.

The Vienna *Ab initio* Simulation Package (VASP) is an optimal candidate for the implementation of unfolding calculations. This code can efficiently deal with large cells, and plane waves are used as basis functions. Moreover, a basic implementation of eq 2 is already available in the recent VASP releases.¹¹ In this work, we extend the original unfolding scheme aiming to reduce the memory requirements and to simplify the user interface for both the input parameters and the extraction of output data. Specifically, we implemented an automatized scheme for generating the supercell reciprocal-space vectors K starting from the given k_i vectors in the primitive cell space. The calculation of the P_{K_m} projection can be limited only to the automatically determined (K, k_i) pairs of interest, saving memory resources in the calculation. The user interface has been simplified, including an automatic initialization of the primitive cell; moreover, the user is provided with a postprocessing package for the analysis of the results, “bands4vasp”,¹² which implements the possibility of graphically visualizing the unfolded energy band structure and spectral functions and includes an algorithm that can determine Fermi wave vectors and Fermi surfaces from folded states with faded Bloch character.

This updated implementation of the unfolding technique in VASP can be applied to a wide range of physical problems: In the following, we describe examples of such applications, starting with an analysis of the electronic states of the Ru-doped BaFe₂As₂ superconductor, a benchmark test to show the reliability and main features of our packages. We continue with an application focused on a novel aspect in the field of catalysis and surface reactivity, the interplay of surface adsorbates with small polarons (i.e., strongly localized in-gap states coupled to lattice phonons). Here the interaction between CO molecules and polarons on the TiO₂(110) surface is revealed by the unfolding scheme, which resolves the small perturbations induced by the adsorbates on the otherwise perfectly flat polaronic bands. Finally, we address the effects of spin fluctuations on the electronic states of EuCd₂As₂: By modeling the phase transition from a noncollinear paramagnetic ordering to ferromagnetic domains and to a complete ferromagnetic order, the progressive removal of the energy degeneracy of the states close to the Fermi level is revealed by means of spectral functions obtained in the framework of the unfolding.

2. METHODOLOGY

Electronic eigenstates calculated for supercells can be unfolded into the reciprocal space of the primitive cell by using external packages based on different methods^{13–17} or directly in VASP, which implements eq 2.^{11,18–20} We have optimized the original implementation in VASP by carefully considering the relation between the K and k_i vectors, as discussed as follows and sketched in Figure 2. At the end of this section, we report a brief description of the bands4vasp postprocessing package¹² that includes convenient visualization tools as well as an algorithm for the automatic identification of Fermi surfaces from supercell folded states with faded Bloch characters.

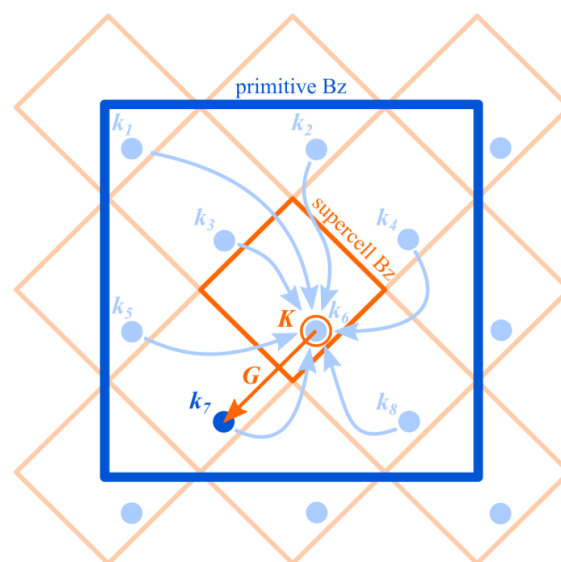


Figure 2. Sketch of the folding problem for a bidimensional $2\sqrt{2} \times 2\sqrt{2}$ supercell. Primitive cell BZ and supercell BZ are represented by large blue and small orange squares, respectively. The arrows indicate the folding of eigenstates from the $|M_{2\sqrt{2} \times 2\sqrt{2}}| = 8$ different k_i primitive cell vectors (filled circles) into one K supercell vector (open, orange circle). The reciprocal lattice vector G highlights the eigenstates unfolding from the K supercell vector to a selected k_i primitive cell vector.

The supercell and the primitive cell are described in terms of 3×3 matrices (A and a , respectively) constructed by the corresponding lattice vectors; similarly, the BZs are defined by matrices (B and b) built by the reciprocal lattice vectors. A transformation matrix M with integer elements relates the supercell and primitive cell in both the direct and reciprocal spaces¹⁹

$$\begin{aligned} A &= Ma \\ B &= (M^{-1})^T b \end{aligned} \quad (3)$$

The determinant $|M|$ of the transformation matrix defines the ratio between the supercell and the primitive cell volumes in the direct (V and v) and reciprocal (W and w) spaces: $|M| = V/v = w/W$. The eigenstates of a single K point in the supercell BZ correspond to eigenstates of the primitive cell folded from different primitive cell points k_i , with i running from 1 to $|M|$. (See Figure 2). These points are connected by linear combinations of supercell reciprocal lattice vectors $\{G\}_i$

$$k_i \leftarrow K + \{G\}_i \text{ with } i = 1, \dots, |M| \quad (4)$$

The folding problem can be equivalently expressed by considering that the eigenstates of one k_i vector fold to one unique K point in the first BZ of the supercell, determined by one specific combination of supercell reciprocal lattice vectors $\{G\}_0$

$$K \leftarrow k_i - \{G\}_0 \quad (5)$$

See also the straight arrow in Figure 2.

The two previous equations allow for an efficient mapping of the supercell and primitive cell reciprocal spaces. We implemented the possibility of limiting the calculation of the Bloch character to specific (K, k_i) pairs fulfilling eq 4 for any supercell K vector defined in the input, excluding all other pairs that would trivially result in $P_{Km}(k_i) = 0$. This restriction considerably reduces the computational effort, as fewer Bloch characters need to be evaluated: The number of evaluated characters for states on any K is given by $|M|$.

Additionally, the calculation of the Bloch character can be further limited to selected k_i vectors of interest. In fact, the user is typically interested in retrieving the eigenstates for selected k_i vectors from the folded supercell states rather than exploring all contributions to the supercell K vectors. Therefore, the k_i vectors can be initialized by the user; then, they are automatically translated into the supercell reciprocal space by the transformation

$$K^B = M k_i^b \quad (6)$$

where K^B and k_i^b represent the vector coordinates expressed in the supercell and primitive cell reciprocal spaces, respectively. The calculation of the Bloch character can then be executed as in the original implementation, but it is limited to (K, k_i) pairs satisfying eq 5. This approach drastically reduces the computational effort of the algorithm because the $P_{Km}(k_i)$ character needs to be evaluated on only one single K for any given k_i . (See also the discussion in the Benchmark and Results section.)

The implementation of these automatized features simplifies the initialization of the unfolding calculation for the user. Moreover, the primitive cell lattice vectors can also be automatically determined from the supercell by the program, by simply inverting eq 3, if the transformation matrix M is specified in input: $a = M^{-1}A$.

The extraction of the output data is quite straightforward as well. To further facilitate the analysis of unfolding calculations, we make available the bands4vasp postprocessing package for band structure analysis.¹² This can also be used for the construction of unfolded band structures, Fermi surfaces, and spectral functions, as well as the automatic calculation of Fermi wave vectors (i.e., the k_i vector of eigenstates at the Fermi level). We recall that in the framework of unfolding calculations, the spectral function A is approximated as

$$A(k, E) = \sum_m P_{Km}(k) \delta(E_m - E) \quad (7)$$

where $\delta(E_m - E)$ are Dirac delta functions centered around E_m energies.

The calculation of Fermi wave vectors needs special consideration in unfolding calculations for supercells that are not built as a perfect stacking of the primitive cell. In this nontrivial case, multiple (up to $|M|$) primitive cell states $|k, n\rangle$ contribute to the supercell state $|Km\rangle$, as revealed by faded $P_{Km}(k_i)$ Bloch characters, typically leading to broad unfolded bands. To identify the crossing of these broad bands with the Fermi level, we adopt a simple procedure: (i) For every k_i vector, the energy eigenvalues in an arbitrary energy range are assigned to a certain energy band by also considering similarities in the orbital symmetry of the eigenstates. (ii) Then, we define a band center of mass by averaging the energy values with weights given by the corresponding $P_{Km}(k_i)$ character. (iii) Finally, the intersection of every band with the Fermi level is found by interpolation. An example of the automatic calculation of Fermi wave vectors and the corresponding Fermi surface is discussed in the next section.

3. BENCHMARK AND RESULTS

We tested our implementation of the unfolding algorithm embedded in VASP by considering the electronic properties of $\text{BaFe}_{2(1-x)}\text{Ru}_x\text{As}_2$ (with $x = 0$ and 0.25 for the undoped and doped cases, respectively). This material is indeed a good testbed because much reference data are available in literature.^{19–21} We also take this opportunity to describe features included in the postprocessing bands4vasp package, such as the visualization of band structures, the Fermi surfaces and spectral function, and the calculation of Fermi wave vectors (Section 3.1). Finally, we show novel and more challenging applications of our approach: By performing calculations on large cells modeling the $\text{TiO}_2(110)$ surface, the unfolding analysis reveals the formation of flat bands originating from in-gap polaronic states that are perturbed by the interaction with CO adsorbates deposited on the material surface (Section 3.2). Moreover, we describe the band splitting occurring in the transition process from noncollinear paramagnetic to ferromagnetic ordering in EuCd_2As_2 (Section 3.3).

3.1. Analysis of Metallic States in $\text{BaFe}_{2(1-x)}\text{Ru}_x\text{As}_2$. The metal-to-superconductor transition driven by Ru doping in the BaFe_2As_2 pnictide has attracted wide interest in both theoretical and experimental communities,^{22–29} and the unfolding technique has proven itself useful to support DFT investigations. One of the most evident results observed from the EBS is the progressive closure of hole pockets upon doping due to a coupling with structural distortions.^{20,21}

We performed spin-unpolarized DFT calculations on BaFe_2As_2 by maintaining a similar computational setup as in ref 19 but by applying the updated version of the unfolding algorithm. We modeled the BaFe_2As_2 structure adopting

supercells of different size (A_2 , A_8 , A_{16}), constructed by applying the following transformation matrices (as described in eq 3)

$$\mathbf{M}_{2,8,16} = \begin{pmatrix} 0 & 1 & 1 \\ 1 & 0 & 1 \\ 1 & 1 & 0 \end{pmatrix}, \begin{pmatrix} 0 & 2 & 2 \\ 2 & 0 & 2 \\ 1 & 1 & 0 \end{pmatrix}, \text{ and } \begin{pmatrix} 0 & 4 & 4 \\ 2 & 0 & 2 \\ 1 & 1 & 0 \end{pmatrix}$$

with determinants $|\mathbf{M}| = 2, 8, 16$, respectively. The \mathbf{M}_2 matrix represents the transformation from the primitive cell to the conventional unit cell for compounds with the body-centered tetragonal $I4/mmm$ space group, such as BaFe_2As_2 .³⁰ We remark that the \mathbf{M} matrix elements are required to be integers in the unfolding formalism, but this requirement does not prevent us from modeling rotations or nontrivial transformations.⁹ In general, no additional theoretical constraint is introduced by our implementation.

We performed a preliminary test by considering the pure (undoped) BaFe_2As_2 crystal and comparing the EBS obtained from the supercell with the bands calculated directly for the primitive cell. In fact, no difference should be observed between the two band structures once the supercell states are unfolded into the reciprocal space of the primitive cell. Figure 3 shows the unfolded bands of the supercell A_2 constructed by

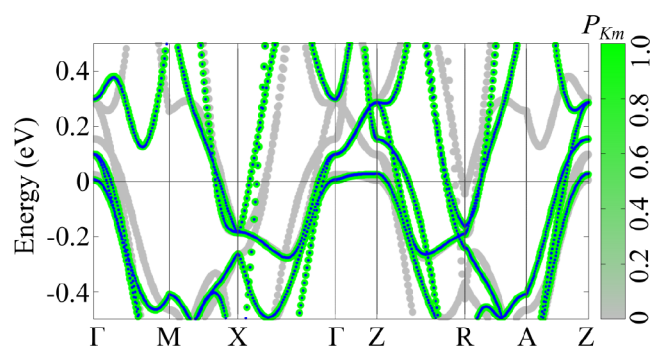


Figure 3. Effective band structure of the supercell constructed by the \mathbf{M}_2 transformation matrix (gray-to-green color gradient) compared with the band structure of the primitive cell (blue).

the transformation matrix \mathbf{M}_2 . As expected (due to $|\mathbf{M}_2| = 2$), we obtained for the supercell twice as many bands as obtained directly from the primitive cell calculation, shown in the figure for comparison. The unfolding algorithm is able to correctly identify the band folding and to assign the Bloch character P_{K_m} accordingly: The gray color in the gradient palette identifies the folded bands with $P_{K_m} = 0$ that belong to different points in the primitive cell reciprocal space. Usually, the folded bands should not be considered in the EBS, and can be omitted from the graph (e.g., by setting the gradient palette with $P_{K_m} = 0$ to the same color as the background of the image).

Figure 4 shows the effects of 25% of Ru doping on the electronic properties of $\text{BaFe}_{2(1-x)}\text{Ru}_{2x}\text{As}_2$ ($x = 0.25$). The band structure in Figure 4a correctly reproduces the closure of the hole pockets around the Γ and Z high-symmetry points.²⁰ The intersection of the bands with the Fermi level can be automatically identified by using the bands4vasp tool: The inset in Figure 4a shows the assignment of the eigenstates around the Fermi energy to different bands (by considering the Bloch character and the orbital symmetry) and the intersection of every band with the Fermi level found by interpolation. This feature is extremely useful for the analysis of the Fermi wave

vectors, which get progressively shortened for the hole pockets around Γ upon Ru doping in this material. Moreover, by collecting all Fermi wave vectors in the BZ, it is possible to construct 3D Fermi surfaces. (See the right panel in Figure 4a.) The 2D cut of the basal plane around Γ (see the inset in Figure 4a) highlights the importance of an accurate sampling of the reciprocal space by comparing the Fermi surface obtained using two different approaches. The right side of the Fermi surface is constructed by using a radial distribution of the k points, leading to a better resolved description of the states around Γ as compared with the resolution obtained by adopting a conventional rectangular grid (left side).

The bands4vasp tool can also extract the atomic orbital character of the eigenstates from unfolding calculations. Figure 4b–d shows the EBSs with Bloch character represented by the size of the circles and the color gradient representing the projection of the states on the d_{yz} (Figure 4b) and $d_{x^2-y^2}$ (Figure 4c) orbitals (essentially due to Fe atoms) and the overall contribution from As atoms (Figure 4d). The contribution of Fe states around Γ (d_{yz} and d_{xz} (not shown here)) and Z ($d_{x^2-y^2}$) and on the BZ border clearly stems from both the band structure and the corresponding 3D Fermi surfaces. Similarly, the hybridization with the As atoms leads to states at the Fermi level around Z and X.

By looking carefully at the $d_{x^2-y^2}$ orbital (in Figure 4c), we note a band crossing the Fermi level in the Γ –Z direction. This feature is highlighted in Figure 5, which shows 2D Fermi surfaces for the basal plane and the parallel planes along Γ –Z obtained for the spectral function $A(\mathbf{k}, E_{\text{Fermi}})$. On the basal plane, only two states appear sharply around Γ (d_{xz} and d_{yz} ; see the orbital analysis on the bottom images in Figure 5a). Conversely, the spectral function for the inner state (with $d_{x^2-y^2}$ orbital symmetry) is absent and becomes progressively better defined when moving toward Z (Figure 5b,c). The spectral function also allows us to easily identify band degeneracy and crossing points between different bands, which are revealed by a more intense value. In Figure 5b, the crossing of the d_{xz} and d_{yz} states determines four points with a large value for the spectral function around the center of the plane. This crossing corresponds to a progressive band switching between d_{xz} and d_{yz} states, clearly identifiable by looking at the evolution of the orbital symmetry of the internal and external rings moving from Γ to Z.

We conclude our benchmark by commenting on the memory requirements of the unfolding algorithm. The automatic determination of $(\mathbf{K}, \mathbf{k}_i)$ pairs (as in eqs 5 and 6) reduces the computational effort by limiting the unfolding procedure only to points of interest. For small systems, such as the A_2 supercell, we counted a memory gain of $\sim 20\%$ when using 300 \mathbf{k} points, which increased to approximately 30 and 50% for the larger A_8 and A_{16} cells, respectively. The lower computational requirements are very useful for performing unfolding calculations that model complex systems. Some original applications of the unfolding method are presented in the following sections.

3.2. In-Gap Polaronic States and Adsorbates on the $\text{TiO}_2(110)$ Surface. The unfolding algorithm can also be applied for DFT calculations on systems with reduced dimensionality, such as the surface slab shown in Figure 6, modeling the pristine rutile $\text{TiO}_2(110)$ termination. Unit cells modeling surfaces of solids in VASP contain a vacuum region to interrupt the periodicity of the system along the surface normal.³¹ Typically, several atomic layers are also included in

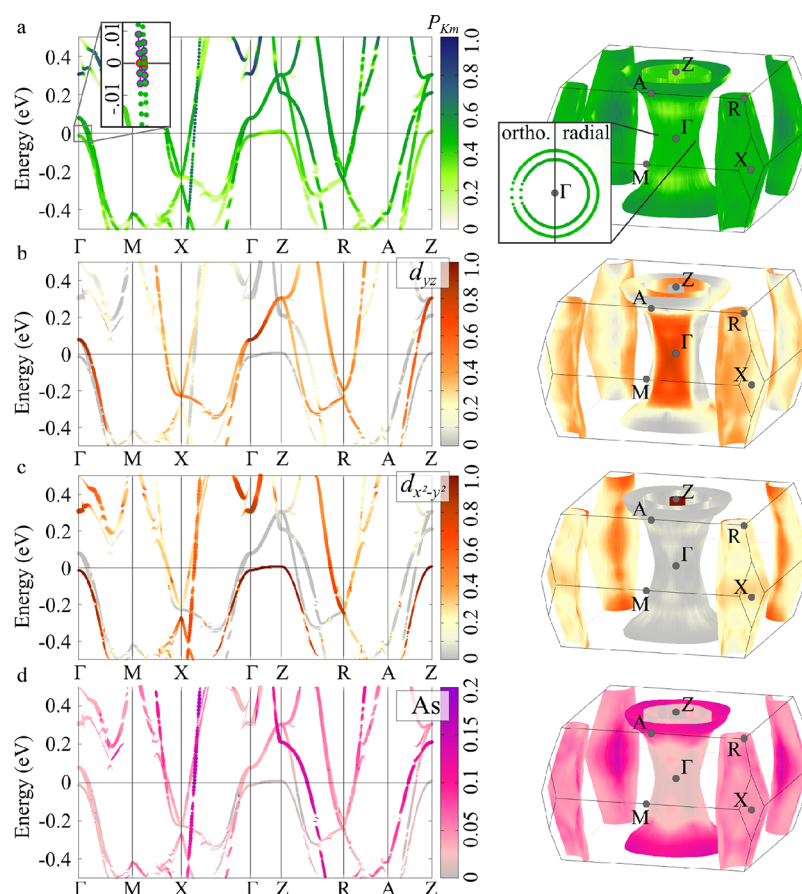


Figure 4. Unfolding for the doped $\text{BaFe}_{2(1-x)}\text{Ru}_{2x}\text{As}_2$ ($x = 0.25$). (a) Effective band structure and 3D Fermi surface. The color gradient indicates the Bloch character. The insets show the identification of the Fermi wave vectors and a 2D cut of the Fermi surface with orthogonal (left) and radial (right) sampling of the reciprocal space. (b–d) Band structures with the Bloch character represented by a variable point sizes with the color gradient indicating the (b) d_{xz} and (c) $d_{x^2-y^2}$ orbital character of Fe atoms and (d) the overall contribution from As atoms. The corresponding 3D Fermi surfaces are also shown.

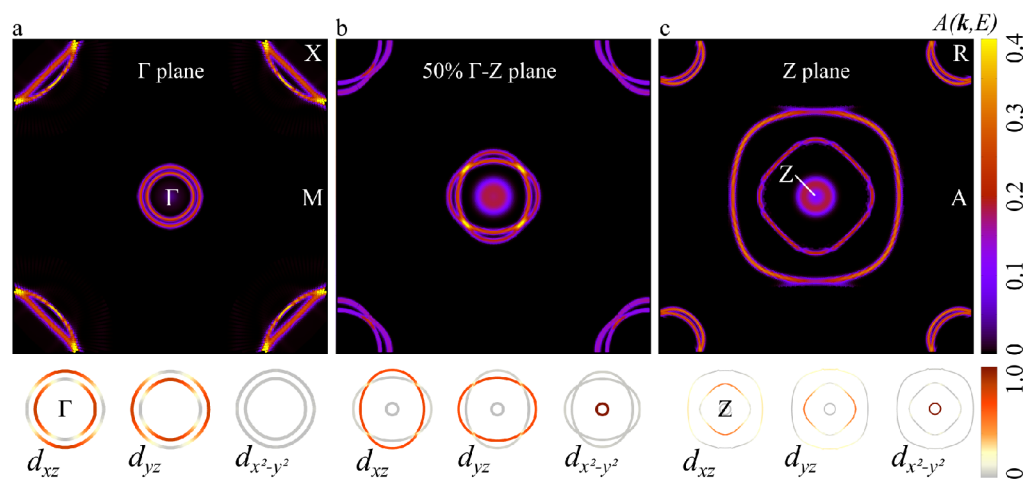


Figure 5. 2D Fermi surfaces calculated using the spectral function $A(\mathbf{k}, E_{\text{Fermi}})$ for (a) the basal plane and (b) the parallel planes halfway in the Γ – Z direction and including (c) the high-symmetry point Z . The corresponding orbital characters of the central rings are shown in the bottom of each panel.

the model to mimic the properties of the bulk below the surface. (See Figure 6a.) Primitive cells and supercells share the same vector perpendicular to the surface, as in Figure 6a. For the modeling of surface reconstructions or defects, supercells are constructed by enlarging the lateral size (see

Figure 6b), leading to folding of electronic states by analogy to the bulk.

Rutile $\text{TiO}_2(110)$ supercells can be used to model the formation of oxygen vacancies on the surface that lead to the stabilization of small electron polarons, that is, electrons strongly localized on Ti ions and coupled to the phonon

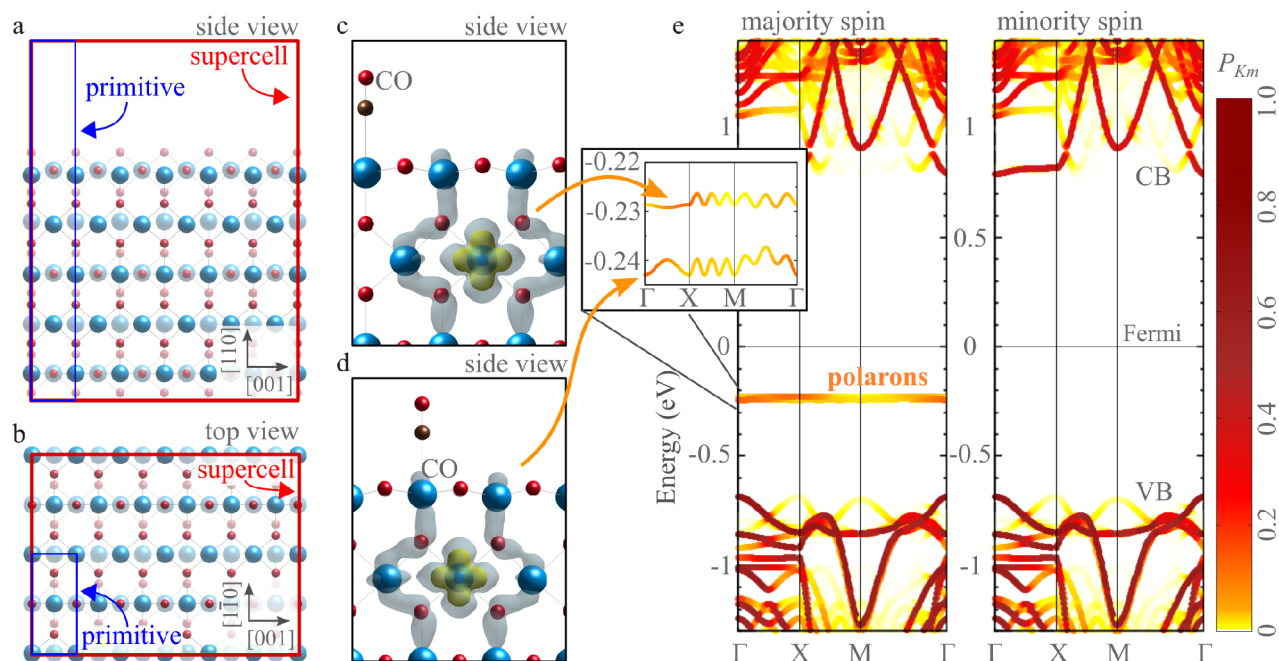


Figure 6. Unfolding for surface slab calculations. (a) Side and (b) top views of the pristine rutile $\text{TiO}_2(110)$ surface. The blue and red rectangles indicate the primitive cell and the 6×2 super cell, respectively. (c,d) Details of the two polarons and the two adsorbed CO molecules. The gray and yellow areas represent the polaronic charge at different isosurface levels. (e) Corresponding effective band structure. The inset shows the detail of the polaronic bands between the conduction (CB) and valence (VB) bands.

field.^{32–34} Small polarons are typically associated with eigenstates appearing in the energy band gap of semiconductors; moreover, polaron localization can occur on different sites with different formation energies.³⁵ (In rutile, subsurface Ti ions are preferred over surface sites.) Polarons are known to drastically affect the electronic and chemical properties of the hosting material, with a substantial impact on the applications. We focus here on the chemical activity of the rutile surface by considering the interplay between polarons and CO adsorbates, recently proposed as the key mechanism for the CO adsorption process on this material.³⁶ The analysis of the unfolded band structure discussed as follows reveals perturbations of the polaronic states that appear as a fingerprint of the polaron–adsorbate interaction.

Figure 6c–e collects the results obtained for large 6×2 supercells containing 363 atoms, including two CO molecules and two polarons. (Technical details of the calculation can be found in ref 36.) As shown in Figure 6c,d, the CO can adsorb on Ti sites at different distances from the polarons. The corresponding EBS (unfolded on the surface primitive cell) shows the appearance of the strongly localized polaronic states, revealed by two flat in-gap bands (one per polaron) in the majority spin channel (Figure 6e). By looking closer at these in-gap bands (inset in Figure 6e), we note that the two polaronic states are not degenerate due to the interaction with the CO molecules. The band appears more perturbed for the polaronic state closer to the CO molecule, as manifested by the increased bandwidth. It is expected that perturbations of the polaronic in-gap states may also originate from the repulsive interaction of polarons at a small distance. In general, a detailed analysis of polaronic and strongly localized electronic states via eigenstate unfolding in supercell calculations might facilitate the interpretation of in-gap states in spectroscopy measurements.^{34,37,38}

3.3. Noncollinear Ferromagnetic Fluctuations in EuCd_2As_2 . We describe here the application of the unfolding algorithm on systems with noncollinear magnetic ordering.¹⁵ We consider the paramagnetic-to-ferromagnetic transition in EuCd_2As_2 , an interesting semimetal showing the emergence of Weyl fermions in the paramagnetic phase due to spin fluctuations of Eu magnetic moments.³⁹ Here we focus on the analysis of the electronic properties of the states around Fermi by considering different magnetic orders and by calculating the corresponding spectral functions, which allows for a clear description of the energy band degeneracy.

Figure 7 compares the effective spectral functions calculated for EuCd_2As_2 with different magnetic orderings. (Technical details of the calculations are described in ref 39.) The paramagnetic phase was modeled by a large supercell including 16 Eu atoms with magnetic moments fixed to random orientations, resulting in a vanishing total magnetization: The corresponding spectral function unfolded in the reciprocal space of the primitive cell is shown in Figure 7a. The flat f bands of Eu atoms appearing around -1.5 eV show an evident incoherence due to the random orientation of the magnetic moments. The three p bands related to the As atoms appear strongly spin-degenerate: The spectral function is very effective in capturing the band degeneracy, as degenerate bands result in higher values of the spectral character, integrating the contribution from every state, as described in eq 7 (at variance with band structures, instead showing the Bloch character of every state individually).

The ferromagnetic phase shows interesting changes (Figure 7c). First, we note that the f bands are more coherent, as expected, due to the ferromagnetic alignment of all Eu magnetic moments. Remarkably, the ferromagnetic order induces a splitting of the p states of As atoms: We indeed observe six bands, lifting the spin degeneracy of the three p

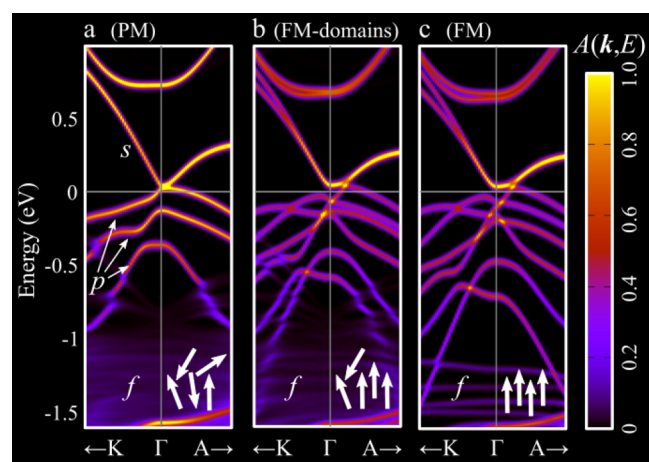


Figure 7. Effective band structure obtained by noncollinear-spin calculations for EuCd_2As_2 considering (a) a paramagnetic phase, (b) ferromagnetic domains, and (c) perfect ferromagnetic ordering. The band structures focus around the Γ point from the K – Γ – A path. The white arrows sketch the arrangement of the magnetic moments of the Eu atoms.

bands in the paramagnetic phase. (Note also the lower spectral function value as compared with the paramagnetic case.)

Although the study of ferromagnetic systems could be done directly in the primitive cell, the supercell approach allowed us to study the paramagnetic-to-ferromagnetic transition by considering ferromagnetic domains embedded in a paramagnetic environment. In Figure 7b, we show the spectral function of the system including a large ferromagnetic domain (consisting of 10 Eu atoms with aligned magnetic moments) and a smaller region (6 atoms) with Eu magnetic moments constrained to random directions. The splitting of the p orbitals persists in this transition state: This is an example of the effect of spin fluctuations on the paramagnetic phase of the compounds. In smaller ferromagnetic domains, the band splitting is gradually reduced, progressively converging toward the paramagnetic degeneracy. (Results obtained by modeling different sizes of the ferromagnetic domain are available in ref 39.)

4. CONCLUSIONS

In summary, we report here our optimization of the unfolding scheme embedded in VASP, characterized by a simplified user interface and reduced memory requirements, thanks to an efficient mapping between the reciprocal spaces of the supercell and primitive cells. The construction of EBSs, spectral functions, Fermi surfaces, and projections of electronic states on orbitals and ions is further facilitated by the bands4vasp postprocessing package.

The unfolding scheme is extremely useful in the interpretation of the results obtained by supercell approaches, and it facilitates the comparison with the experimental observations, especially in the field of spectroscopy. The application range is very broad. We take here the $\text{BaFe}_{2(1-x)}\text{Ru}_{2x}\text{As}_2$ superconductor as a benchmark, given the large amount of data available in the literature. Moreover, we considered the adsorption of CO molecules on the rutile $\text{TiO}_2(110)$ surface to show the suitability of the algorithm for very large supercells, such as those required in surface science calculations. In this case study, the EBS highlights the interactions of adsorbates with strongly localized polarons,

revealed by the perturbation of the flat polaronic bands. Finally, we performed noncollinear calculations for the EuCd_2As_2 semimetal. The supercell approach allowed us to model the paramagnetic phase by constraining magnetic moments along random directions, resulting in a vanishing total magnetization. The corresponding spectral function reveals the spin degeneracy of shallow states below the Fermi level that is lifted by including spin fluctuations via the formation of ferromagnetic domains.

The implementation of the unfolding algorithm proposed here represents a useful computational tool for a wide range of physical and chemical phenomena requiring very large supercells. Thanks to the improved interface, the reduced computational requirements, and the integrated analysis package, these now become easily accessible.

AUTHOR INFORMATION

Corresponding Author

Michele Reticcioli – Faculty of Physics and Center for Computational Materials Science, University of Vienna, 1090 Vienna, Austria; orcid.org/0000-0001-8223-9928; Email: michele.reticcioli@univie.ac.at

Authors

David Dirnberger – Faculty of Physics and Center for Computational Materials Science, University of Vienna, 1090 Vienna, Austria

Georg Kresse – Faculty of Physics and Center for Computational Materials Science, University of Vienna, 1090 Vienna, Austria; VASP Software GmbH, 1090 Vienna, Austria

Cesare Franchini – Faculty of Physics and Center for Computational Materials Science, University of Vienna, 1090 Vienna, Austria; Dipartimento di Fisica e Astronomia, Università di Bologna, 40127 Bologna, Italy; orcid.org/0000-0002-7990-2984

Complete contact information is available at: <https://pubs.acs.org/10.1021/acs.jpcc.1c02318>

Notes

The authors declare no competing financial interest.

ACKNOWLEDGMENTS

This project has benefited from intensive discussions with D. D. Sarma during his visiting professorship in Vienna in spring 2018, during which he elaborated on the concept of electronic state unfolding in a much-appreciated lecture. This work was supported by the joint FWF and Indian Department of Science and Technology (DST) project INDOX (project no. I1490-N19). The computational results presented have been achieved using the Vienna Scientific Cluster (VSC).

REFERENCES

- (1) Shanthi, N.; Sarma, D. D. Electronic structure of electron doped SrTiO_3 : $\text{SrTiO}_{3-\delta}$ and $\text{Sr}_{1-x}\text{La}_x\text{TiO}_3$. *Phys. Rev. B: Condens. Matter Mater. Phys.* **1998**, *57*, 2153–2158.
- (2) Hine, N. D. M.; Frensch, K.; Foulkes, W. M. C.; Finnis, M. W. Supercell size scaling of density functional theory formation energies of charged defects. *Phys. Rev. B: Condens. Matter Mater. Phys.* **2009**, *79*, 024112.
- (3) Ku, W.; Berlijn, T.; Lee, C. C. Unfolding first-principles band structures. *Phys. Rev. Lett.* **2010**, *104*, 216401.

- (4) Day, R. P.; Zwartsenberg, B.; Elfimov, I. S.; Damascelli, A. Computational framework chinook for angle-resolved photoemission spectroscopy. *npj Quantum Materials* **2019**, *4*, 54.
- (5) Hoekstra, H.; Fuggle, J.; Speier, W.; Sarma, D. Matrix elements in appearance potential spectroscopy of Al and its alloys. *J. Electron Spectrosc. Relat. Phenom.* **1987**, *42*, 27–38.
- (6) Popescu, V.; Zunger, A. Effective band structure of random alloys. *Phys. Rev. Lett.* **2010**, *104*, 236403.
- (7) Popescu, V.; Zunger, A. Extracting E versus k effective band structure from supercell calculations on alloys and impurities. *Phys. Rev. B: Condens. Matter Mater. Phys.* **2012**, *85*, 085201.
- (8) Boykin, T. B.; Kharche, N.; Klimeck, G.; Korkusinski, M. Approximate bandstructures of semiconductor alloys from tight-binding supercell calculations. *J. Phys.: Condens. Matter* **2007**, *19*, 036203.
- (9) Boykin, T. B.; Kharche, N.; Klimeck, G. Brillouin-zone unfolding of perfect supercells having nonequivalent primitive cells illustrated with a Si/Ge tight-binding parameterization. *Phys. Rev. B: Condens. Matter Mater. Phys.* **2007**, *76*, 035310.
- (10) Voit, J.; Perfetti, L.; Zwick, F.; Berger, H.; Margaritondo, G.; Gruner, G.; Hochst, H.; Grioni, M. Electronic structure of solids with competing periodic potentials. *Science* **2000**, *290*, 501–503.
- (11) Eckhardt, C.; Hummer, K.; Kresse, G. Indirect-to-direct gap transition in strained and unstrained SnxGe_{1-x} alloys. *Phys. Rev. B: Condens. Matter Mater. Phys.* **2014**, *89*, 165201.
- (12) Dirnberger, D.; Kresse, G.; Franchini, C.; Reticcioli, M. bands4vasp Post-Processing Package, 2021. <https://github.com/QuantumMaterialsModelling/bands4vasp> (accessed 2021-05-26).
- (13) Zheng, F.; Zhang, P.; Duan, W. Quantum Unfolding: A program for unfolding electronic energy bands of materials. *Comput. Phys. Commun.* **2015**, *189*, 213–219.
- (14) Medeiros, P. V.; Stafström, S.; Björk, J. Effects of extrinsic and intrinsic perturbations on the electronic structure of graphene: Retaining an effective primitive cell band structure by band unfolding. *Phys. Rev. B: Condens. Matter Mater. Phys.* **2014**, *89*, 041407.
- (15) Medeiros, P. V.; Tsirkin, S. S.; Stafström, S.; Björk, J. Unfolding spinor wave functions and expectation values of general operators: Introducing the unfolding-density operator. *Phys. Rev. B: Condens. Matter Mater. Phys.* **2015**, *91*, 041116.
- (16) Herath, U.; Tavazde, P.; He, X.; Bousquet, E.; Singh, S.; Muñoz, F.; Romero, A. H. PyProcar: A Python library for electronic structure pre/post-processing. *Comput. Phys. Commun.* **2020**, *251*, 107080.
- (17) Wang, V.; Xu, N.; Liu, J. C.; Tang, G.; Geng, W.-T. VASPKIT: A User-friendly Interface Facilitating High-throughput Computing and Analysis Using VASP Code. *arXiv* **2019**, 1–26, DOI: 10.1016/j.cpc.2021.108033.
- (18) Liu, P.; Reticcioli, M.; Kim, B.; Continenza, A.; Kresse, G.; Sarma, D. D.; Chen, X. Q.; Franchini, C. Electron and hole doping in the relativistic Mott insulator Sr_2IrO_4 : A first-principles study using band unfolding technique. *Phys. Rev. B: Condens. Matter Mater. Phys.* **2016**, *94*, 195145.
- (19) Reticcioli, M.; Profeta, G.; Franchini, C.; Continenza, A. Effective band structure of Ru-doped BaFe_2As_2 . *J. Phys.: Conf. Ser.* **2016**, *689*, 012027.
- (20) Reticcioli, M.; Profeta, G.; Franchini, C.; Continenza, A. Ru doping in iron-based pnictides: The “unfolded” dominant role of structural effects for superconductivity. *Phys. Rev. B: Condens. Matter Mater. Phys.* **2017**, *95*, 214510.
- (21) Wang, L.; Berlijn, T.; Wang, Y.; Lin, C. H.; Hirschfeld, P. J.; Ku, W. Effects of disordered Ru substitution in BaFe_2As_2 : Possible realization of superdiffusion in real materials. *Phys. Rev. Lett.* **2013**, *110*, 037001.
- (22) Thaler, A.; Ni, N.; Kracher, A.; Yan, J. Q.; Bud'ko, S. L.; Canfield, P. C. Physical and magnetic properties of $\text{Ba}(\text{Fe}_{1-x}\text{Ru}_x)\text{As}_2$ single crystals. *Phys. Rev. B: Condens. Matter Mater. Phys.* **2010**, *82*, 014534.
- (23) Sharma, S.; Bharathi, A.; Chandra, S.; Reddy, V. R.; Paulraj, S.; Satya, A. T.; Sastry, V. S.; Gupta, A.; Sundar, C. S. Superconductivity in Ru-substituted polycrystalline $\text{BaFe}_{2-x}\text{Ru}_x\text{As}_2$. *Phys. Rev. B: Condens. Matter Mater. Phys.* **2010**, *81*, 174512.
- (24) Eom, M. J.; Na, S. W.; Hoch, C.; Kremer, R. K.; Kim, J. S. Evolution of transport properties of $\text{BaFe}_{2-x}\text{Ru}_x\text{As}_2$ in a wide range of isovalent Ru substitution. *Phys. Rev. B: Condens. Matter Mater. Phys.* **2012**, *85*, 024536.
- (25) Kim, M. G.; Soh, J.; Lang, J.; Dean, M. P. M.; Thaler, A.; Bud'ko, S. L.; Canfield, P. C.; Bourret-Courchesne, E.; Kreyssig, A.; Goldman, A. I.; Birgeneau, R. J. Spin polarization of Ru in superconducting $\text{Ba}(\text{Fe}_{0.795}\text{Ru}_{0.205})\text{As}_2$ studied by x-ray resonant magnetic scattering. *Phys. Rev. B: Condens. Matter Mater. Phys.* **2013**, *88*, 014424.
- (26) Sharma, S.; Bharathi, A.; Vinod, K.; Sundar, C. S.; Srihari, V.; Sen, S.; Ghosh, H.; Sinha, A. K.; Deb, S. K. Structural investigations in $\text{BaFe}_2 - \text{X Ru}_x\text{As}_2$ as a function of Ru and temperature. *Acta Crystallogr., Sect. B: Struct. Sci., Cryst. Eng. Mater.* **2015**, *71*, 61–67.
- (27) Devidas, T. R.; Mani, A.; Sharma, S.; Vinod, K.; Bharathi, A.; Sundar, C. S. Unification of the pressure and composition dependence of superconductivity in Ru substituted BaFe_2As_2 . *Solid State Commun.* **2014**, *185*, 62–66.
- (28) Sen, S.; Ghosh, H.; Sinha, A. K.; Bharathi, A. Origin of structural and magnetic transitions in $\text{BaFe}_2\text{-xRu}_x\text{As}_2$ materials. *Supercond. Sci. Technol.* **2014**, *27*, 122003.
- (29) Liu, L.; Mikami, T.; Ishida, S.; Koshiishi, K.; Okazaki, K.; Yoshida, T.; Suzuki, H.; Horio, M.; Ambolode, L. C.; Xu, J.; et al. In-plane electronic anisotropy in the antiferromagnetic orthorhombic phase of isovalent-substituted $\text{Ba}(\text{Fe}_{1-x}\text{Ru}_x)\text{As}_2$. *Phys. Rev. B: Condens. Matter Mater. Phys.* **2015**, *92*, 094503.
- (30) Setyawan, W.; Curtarolo, S. High-throughput electronic band structure calculations: Challenges and tools. *Comput. Mater. Sci.* **2010**, *49*, 299–312.
- (31) Sholl, D. S.; Steckel, J. A. DFT Calculations for Surfaces of Solids. *Density Functional Theory* **2009**, 83–112.
- (32) Setvin, M.; Franchini, C.; Hao, X.; Schmid, M.; Janotti, A.; Kaltak, M.; Van De Walle, C. G.; Kresse, G.; Diebold, U. Direct view at excess electrons in TiO_2 rutile and anatase. *Phys. Rev. Lett.* **2014**, *113*, 086402.
- (33) Rousseau, R.; Glezakou, V. A.; Selloni, A. Theoretical insights into the surface physics and chemistry of redox-active oxides. *Nature Reviews Materials* **2020**, *5*, 460–475.
- (34) Franchini, C.; Reticcioli, M.; Setvin, M.; Diebold, U. Polarons in materials. *Nature Reviews Materials* **2021**, *689*, 012027.
- (35) Reticcioli, M.; Setvin, M.; Schmid, M.; Diebold, U.; Franchini, C. Formation and dynamics of small polarons on the rutile TiO_2 (110) surface. *Phys. Rev. B: Condens. Matter Mater. Phys.* **2018**, *98*, 045306.
- (36) Reticcioli, M.; Sokolović, I.; Schmid, M.; Diebold, U.; Setvin, M.; Franchini, C. Interplay between Adsorbates and Polarons: CO on Rutile TiO_2 (110). *Phys. Rev. Lett.* **2019**, *122*, 016805.
- (37) Mao, Y.; Ma, X.; Wu, D.; Lin, C.; Shan, H.; Wu, X.; Zhao, J.; Zhao, A.; Wang, B. Interfacial Polarons in van der Waals Heterojunction of Monolayer SnSe 2 on SrTiO_3 (001). *Nano Lett.* **2020**, *20*, 8067–8073.
- (38) Santander-Syro, A. F.; Bareille, C.; Fortuna, F.; Copie, O.; Gabay, M.; Bertran, F.; Taleb-Ibrahimi, A.; Le Fèvre, P.; Herranz, G.; Reyren, N.; et al. Orbital symmetry reconstruction and strong mass renormalization in the two-dimensional electron gas at the surface of KTaO_3 . *Phys. Rev. B: Condens. Matter Mater. Phys.* **2012**, *86*, 121107.
- (39) Ma, J. Z.; Nie, S. M.; Yi, C. J.; Jandke, J.; Shang, T.; Yao, M. Y.; Naamneh, M.; Yan, L. Q.; Sun, Y.; Chikina, A.; et al. Spin fluctuation induced Weyl semimetal state in the paramagnetic phase of EuCd_2As_2 . *Science Advances* **2019**, *5*, eaaw4718.